HSPI The Open Access Publisher

J R O JOURNAL OF RADIOLOGY AND ONCOLOGY
ISSN 2573-7724

Review Article

Contrast-enhanced Susceptibility Weighted Imaging (CE-SWI) for the Characterization of Musculoskeletal Oncologic Pathology: A Pictorial Essay on the Initial Five-year Experience at a Cancer Institution

Raul F Valenzuela[1]*, E Duran-Sierra[2], MA Canjirathinkal[2], B Amini[2], J Ma[2], KP Hwang[2], RJ Stafford[2], Keila E Torres[2], MA Zarzour[2], JA Livingston[2], JE Madewell[2], WA Murphy[2] and CM Costelloe[2]

[1]Department of Musculoskeletal Imaging, University of Texas MD Anderson Cancer Center, USA
[2]Houston, Texas, USA

Abstract

Susceptibility-weighted imaging (SWI) is based on a 3D high-spatial-resolution, velocity-corrected gradient-echo MRI sequence that uses magnitude and filtered-phase information to create images. It SWI uses tissue magnetic susceptibility differences to generate signal contrast that may arise from paramagnetic (hemosiderin), diamagnetic (minerals and calcifications) and ferromagnetic (metal) molecules. Distinguishing between calcification and blood products is possible through the filtered phase images, helping to visualize osteoblastic and osteolytic bone metastases or demonstrating calcifications and osteoid production in liposarcoma and osteosarcoma. When acquired in combination with the injection of an exogenous contrast agent, contrast-enhanced SWI (CE-SWI) can simultaneously detect the T2* susceptibility effect, T2 signal difference, contrast-induced T1 shortening, and out-of-phase fat and water chemical shift effect. Bone and soft tissue lesion SWI features have been described, including giant cell tumors in bone and synovial sarcomas in soft tissues. We expand on the appearance of benign soft-tissue lesions such as hemangioma, neurofibroma, pigmented villonodular synovitis, abscess, and hematoma. Most myxoid sarcomas demonstrate absent or just low-grade intra-tumoral hemorrhage at the baseline. CE-SWI shows superior differentiation between mature fibrotic T2* dark components and active enhancing T1 shortening components in desmoid fibromatosis. SWI has gained popularity in oncologic MSK imaging because of its sensitivity for displaying hemorrhage in soft tissue lesions, thereby helping to differentiate benign versus malignant soft tissue tumors. The ability to show the viable, enhancing portions of a soft tissue sarcoma separately from hemorrhagic/necrotic components also suggests its utility as a biomarker of tumor treatment response. It is essential to understand and appreciate the differences between spontaneous hemorrhage patterns in high-grade sarcomas and those occurring in the therapy-induced necrosis process in responding tumors. Ring-like hemosiderin SWI pattern is observed in successfully treated sarcomas. CE-SWI also demonstrates early promising results in separating the T2* blooming of healthy iron-loaded bone marrow from the T1-shortened enhancement in bone marrow that is displaced by the tumor.

SWI and CE-SWI in MSK oncology learning objectives:

SWI and CE-SWI can be used to identify calcifications on MRI.

Certain SWI and CE-SWI patterns can correlate with tumor histologic type.

CE-SWI can discriminate mature from immature components of desmoid tumors.

CE-SWI patterns can help to assess treatment response in soft tissue sarcomas.

Understanding CE-SWI patterns in post-surgical changes can also be useful in discriminating between residual and recurrent tumors with overlapping imaging features.

More Information

***Address for correspondence:** Raul F Valenzuela, MD, Department of Musculoskeletal Imaging, University of Texas MD Anderson Cancer Center, 1515 Holcombe Blvd., Unit 1475, Houston, TX 77030-4009, USA, Email: rfvalenzuela@mdanderson.org

https://orcid.org/0000-0002-2597-8537

Submitted: February 26, 2024
Approved: April 01, 2024
Published: April 02, 2024

How to cite this article: Valenzuela RF, Duran-Sierra E, Canjirathinkal MA, Amini B, Ma J, et al. Contrast-enhanced Susceptibility Weighted Imaging (CE-SWI) for the Characterization of Musculoskeletal Oncologic Pathology: A Pictorial Essay on the Initial Five-year Experience at a Cancer Institution. J Radiol Oncol. 2024; 8: 030-045.

DOI: 10.29328/journal.jro.1001062

Keywords: Soft tissue sarcoma; Undifferentiated pleomorphic sarcoma; Multiparametric MRI; Treatment-induced hemorrhage; Susceptibility-weighted imaging

Abbreviations: ADC: Apparent Diffusion Coefficient; ABASTI: Advanced Bone and Soft-Tissue Imaging; ALT: Atypical Lipomatous Tumor; CE: Contrast-Enhanced; CE-SWI: Contrast Enhanced Susceptibility-Weighted Imaging; CR: Complete Ring; DCE: Dynamic Contrast-Enhanced; DWI: Diffusion-Weighted Imaging; FS: Fat-Suppressed; LMS: Leiomyosarcoma; Min IP: Minimum Intensity Projection; MRI: Magnetic Resonance Imaging; SWI: Susceptibility-Weighted Imaging; STS: Soft Tissue Sarcoma; T1W, T1: Weighted; T2W, T2: Weighted; UPS: Undifferentiated Pleomorphic Sarcoma; VOI: Volume of Interest; RECIST: Response Evaluation Criteria in Solid Tumors; WHO: World Health Organization

Introduction

Susceptibility-Weighted Imaging (SWI)

Is based on a 3D high-spatial-resolution, velocity-corrected gradient-echo MRI sequence that uses magnitude and filtered-phase information to create images [1,2]. SWI uses tissue magnetic susceptibility differences to generate signal contrast. Such signal arises from paramagnetic (hemosiderin), diamagnetic (oxyhemoglobin, minerals, and calcifications), and ferromagnetic (metal) molecules. All these molecules cause loss of the signal amplitude and similar T2* hypo intensity. Typically, the paramagnetic deoxyhemoglobin serves as an intrinsic contrast agent on SWI sequences with its characteristic low T2* signal.

SWI-phase: Although paramagnetic, diamagnetic, and ferromagnetic molecules can cause SWI amplitude-related T2* hypo intensity, using SWI-Phase information, diamagnetic molecules can be differentiated from the rest. Signature phase changes [1-3] can be exploited and analyzed for the underlying tissue susceptibility differences. Paramagnetic substances (deoxygenated hemoglobin, intracellular methemoglobin, hemosiderin, and ferritin) display positive phase shift and hypo intensity in left-handed MR systems. In contrast, the diamagnetic effects of calcium or oxyhemoglobin could display a negative shift with hyperintensity. Most importantly, in a right-handed system, veins look dark on phase images because it is paramagnetic relative to surrounding tissues. Meanwhile, calcium looks bright on phase images because it is diamagnetic relative to surrounding tissues. The latter is clinically helpful in characterizing calcifications, as further discussed in section 2 [4-7].

Aliasing: Although filtered phase images (SWI-Phase) are sensitive to minimal amounts of calcium, they can be confusing when more significant amounts of calcification or hemosiderin are present. Large regions of calcifications can have dark areas or be surrounded by dark regions. The converse is also seen in large areas of profound hemosiderin staining [8].

SWI and SWI Min IP: SWI images are often displayed as minimum intensity projections (MIP). The diamagnetic or paramagnetic foci are seen as being bright or dark depending on the phase mask used [9]. The actual implementation of SWI on each scanner is optimized by the manufacturer for the best contrast. Oftentimes, it is possible to determine the implementation of an individual scanner by observing the appearance of paramagnetic structures and blood vessels, with diamagnetic structures displaying the opposite appearance [10].

CE-SWI: Contrast-enhanced susceptibility-weighted imaging (CE-SWI) is gaining popularity in oncologic MSK imaging because of its sensitivity to hemorrhage in soft tissue lesions that can help with tumor grading and differentiating benign versus malignant soft tissue tumors. **CE-SWI** can combine the benefits of SWI in the detection of hemorrhage-related T2* susceptibility effect and the advantages of contrast enhancement such as in distinguishing the necrotic fluid T2 signal from the contrast-induced T1 shortening of viable enhancing tumor [12-15].

SWI and CE-SWI applications

Non-Tumoral MSK applications: Most publications referring to non-tumoral SWI applications describe them without the use of intravenous contrast (CE-SWI). Suggested potential non-tumor applications of SWI in MSK imaging include joint disorders, fracture detection, and degenerative disc disease [8]. SWI has shown promising results for applications such as ruling out rotator cuff calcific tendinopathy, characterization of sub-coracoacromial spurs in the setting of subacromial impingement syndrome, differentiation between disc protrusion or extrusion versus osteophyte, evaluation of vertebral body fractures, and in the assessment of bone trabecular pattern within vertebral hemangiomas [3,15-18]. In the MSK system, SWI has been studied for the identification of calcifications in tendons [15] and spurs [16], osteophytes [17], joint erosions [19], hemarthrosis [20], meniscal trauma [21], vertebral fractures [22], bone metastases [18] and sclerotic bone lesions [3].

MSK oncology applications: SWI and CE-SWI have gained popularity in oncologic MSK imaging because of their sensitivity to blood metabolites in soft tissue lesions. This can help in the differentiation of benign versus malignant soft tissue tumors because many malignant soft tissue tumors demonstrate hemorrhage distributed primarily in the central region of the tumor [23]. Some bone and soft tissue tumor SWI features have already been described, including giant cell tumors of bone and synovial sarcomas of the soft tissues [23-25]. This review represents the initial presentation of several bone and soft-tissue tumors to highlight the diagnostic value of SWI and CE-SWI. Useful susceptibility artifacts are seen in high-grade tumors and benign entities such as pigmented villonodular synovitis or hematoma [26,27]. Further knowledge about SWI and CE-SWI patterns may help to guide treatment decisions and help to characterize histology-specific tumor signatures.

Contrast-enhanced Susceptibility Imaging (CE-SWI) sequence parameters: Our institution has a fleet of 29 MR scanners from two manufacturers that are used to perform standardized CE-SWI sequences. Parameters were tailored according to MRI vendor and field strength. Siemens (Siemens Healthineers, Erlangen, Germany) uses a phase-filtered approach, which applies a weighting based on susceptibility-induced phase changes. In contrast, GEHC (GE Healthcare, Milwaukee, WI) uses a magnitude averaging approach that combines echoes with varying echo times. Scanners at 3T field strength utilize shorter echo times and

repetition times compared to 1.5T scanners due to the more significant susceptibility effect at higher field strength. The typical scan parameters that are used at our institution across all magnets are as follows: repetition time (TR) = 27-78 msec, echo- time (TE) = 20-49 msec, frequency encode step = 256-300, phase encode step = 186-256, slice thickness = 5mm, and flip angle (FA) = 15°. The cases presented in this review were collected from our routine clinical oncologic MSK MRI practice from 2019 to 2024.

Qualitative and quantitative SWI features have been shown to differentiate viable tissue from hemorrhagic/ necrotic components in soft tissue sarcomas, highlighting its potential utility for assessing tumor treatment response [26,27]. Therefore, understanding and appreciating the differences between the spontaneous hemorrhage patterns often seen in therapy-naive high-grade sarcomas from those occurring in the therapy-induced necrosis process in responding tumors [26-30] may be relevant.

SWI/CE-SWI and calcifications

Most conventional MR sequences rely on differences between the longitudinal spin relaxation (T1) and the transverse spin relaxation (T2) times of the tissues for image contrast [10]. These sequences cannot distinguish between calcium and blood because both reduce the relaxation times similarly [10]. The most common use of SWI is to identify small amounts of bleeding or calcium, which may be difficult or subtle on conventional MRI sequences. Distinguishing between calcification and blood products is impossible on the post-processed SWI images because both can demonstrate signal drop-out and bloom. Nevertheless, the filtered phase images can be helpful in this regard, because diamagnetic and paramagnetic compounds affect signal phase differently, causing hemorrhage and calcification to appear with signal intensity opposite to each other [1,2]. Utilization of the filtered phase images for identifying calcium may lead to reliable differentiation between osteoblastic and osteolytic spine metastases with an accuracy that is superior to the standard spine MRI sequences [3]. Accurately detecting calcifications is essential because they can provide clues to the nature of pathologic or post-traumatic processes. CT or radiography are typically used for this purpose. However, both modalities expose patients to ionizing radiation and cannot provide the superior soft tissue resolution of MRI. Adams, et al. conducted a meta-analysis to determine the potential of SWI, compared to conventional MRI, to identify calcifications in the brain and soft tissues of the body using CT as the reference standard. They found that SWI had superior sensitivity and comparable specificity to traditional MRI [31]. Described clinical applications including the characterization of tumor calcification in brain Oligodendrogliomas [32].

SWI and skeletal non-tumoral calcifications: Norenberg, et al. studied SWI in the rotator cuff and reported that 98% of the tendinous calcifications were correctly identified with SWI [15]. Limitations of SWI include the blooming artifact that may lead to an overestimate of the size of the calcifications and lower spatial resolution than conventional sequences [9]. Norenberg, et al. also studied spurs in patients suspected of having subacromial impingement syndrome. The authors report that SWI allows reliable detection of subacromial spurs and is superior to conventional MRI for this indication [16]. Bender, et al. conducted a prospective study on patients with suspected spinal radiculopathy and found that most osteophytes were correctly identified on SWI [17].

SWI and CE-SWI skeletal tumor calcifications: Densely calcified or ossified lesions tend to lower the enhancement of the lesions on contrast-enhanced SWI images (CE-SWI). Osteoblastic lesions, periosteal ossification, or cortical hyperostosis can appear dark in CE-SWI and bright on phase imaging. Low-grade liposarcoma can have a predominant proportion of well or semi-well-differentiated lipomatous tissue combined with various degrees of soft tissue components and calcifications [33].

On CE-SWI phase imaging, intratumoral calcifications may appear dark on magnitude-weighted images and bright on phase images (Figure 1), analogous to brain oligodendriomas [11,31]. Osteoblastic osteosarcoma, with a periosteal soft tissue component, can demonstrate a dense “sunburst” periosteal mineralization/ “hair-on end” periosteal calcifications, can appear dense on CT and radiography, dark in the SWI imaging, and bright with “blooming” in phase imaging (Figure 2) [11,35]. Such a phenomenon facilitates the differentiation of calcification over hemorrhage. MR imaging that recapitulates the appearance of calcium on CT and radiography is expected to gain relevance in clinical practice [10].

CE-SWI in benign soft tissue masses

Soft-tissue abscesses (Figure 3), neurofibromas (Figure 4) and hemangiomas (Figure 5) may demonstrate specific CE-SWI signatures [9].

Intramuscular abscess: In the oncologic practice, muscular abscesses tend to occur in immunocompromised individuals such as leukemic patients, particularly AML. In its early phases, they demonstrate a “ring-like” hypervascularity on DCE dynamic imaging and central restricted diffusion on ADC maps. Once the lesion starts healing, a more solid-like enhancement is observed, and a clear T2* hypointense peripheral ring develops in the CE-SWI sequence (Figure 3). This finding resembles the one described in patients with brain pyogenic abscesses [11].

Benign Peripheral Nerve Sheath Tumor (BPNST): CE-SWI can demonstrate a complex**,** layered appearance with central areas of low T2* linear and dot-like susceptibility, possibly reflecting slow-flowing veins and fibrous stroma. It displays alternating high and low signal layers caused by

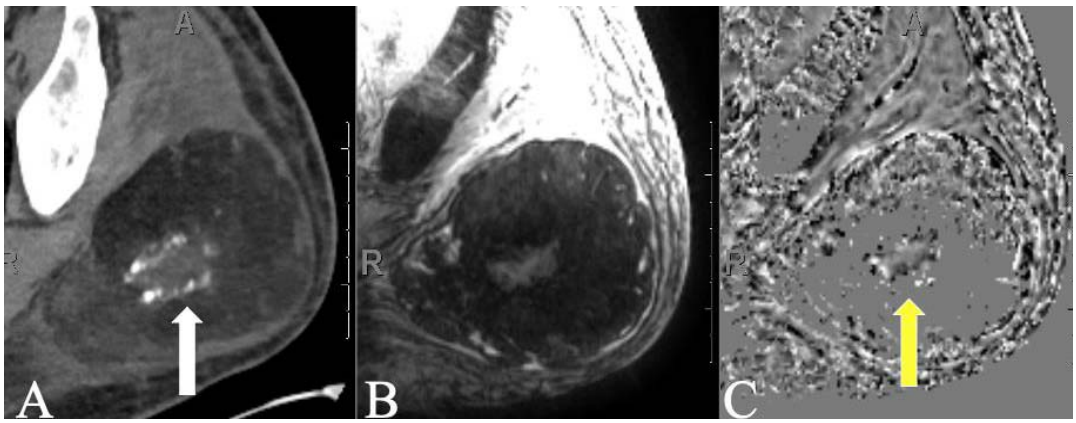

Figure 1: Liposarcomas and soft-tissue calcifications. (A) CT of the left buttock demonstrates a lipomatous mass with central calcifications (white arrow). (B) Post-contrast Dixon water sequence demonstrating low-grade central enhancement and homogenous peripheral fat saturation. The calcifications are not identifiable on conventional MRI. (C) SWI-phase imaging demonstrates central hyperintense calcification (yellow arrow). Using this method, calcifications are detectable on MRI. Figure modified from RF Valenzuela, et al. [11].

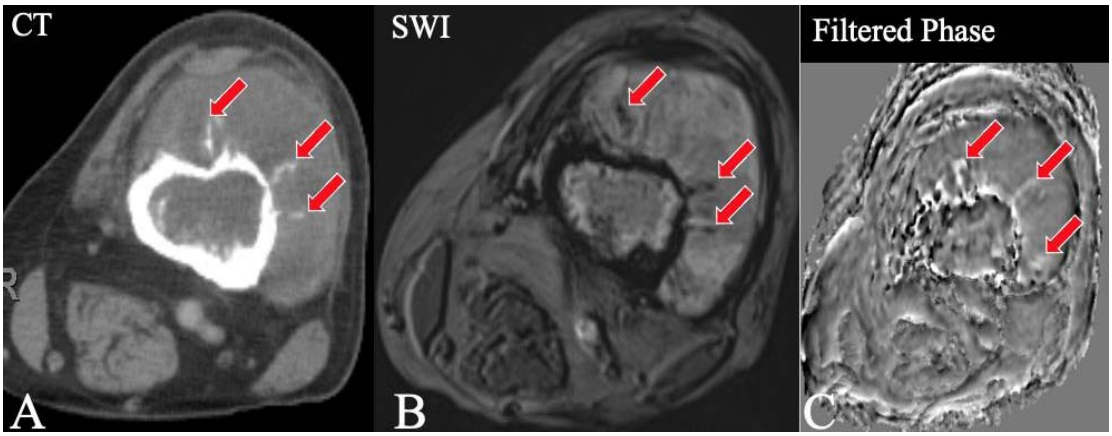

Figure 2: SWI calcium detection in osteosarcoma-related "hair-on-end" periosteal reaction. Osteosarcoma arising from the left distal femur. (A) CT axial imaging demonstrates osteosarcoma of the distal femoral meta-diaphysis associated with a significant soft-tissue component with radial "hair-on-end" periosteal calcifications (red arrows). (B) SWI-CE (combined magnitude and filtered phase) demonstrates that the calcifications show linear T2* hypo intensity (red arrows) that could be mistakenly interpreted as hemorrhage. (C) On SWI-phase (filtered phase imaging), the radial "hair-on-end" calcifications demonstrate linear hyperintensity (red arrows) that mimics their appearance on CT. Figure modified from RF Valenzuela, et al. [11].

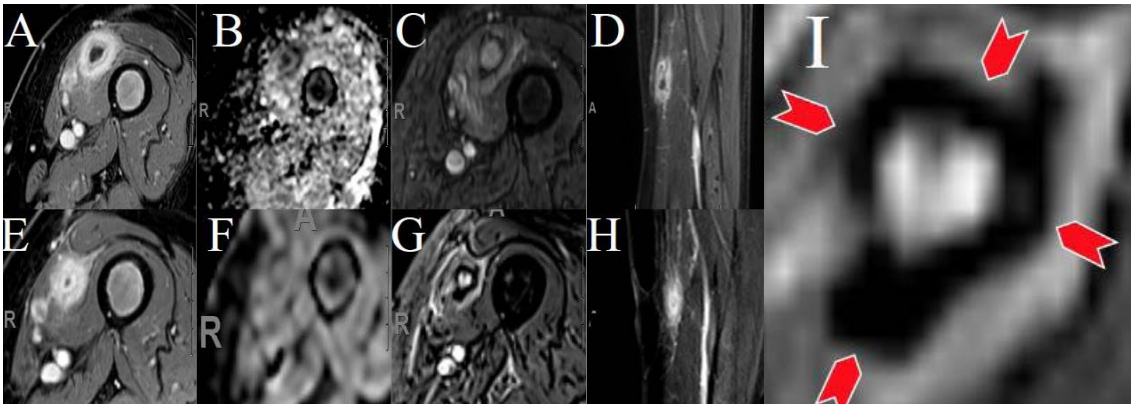

Figure 3: Intramuscular abscess in a patient with Acute Myeloblastic Leukemia: Initial MRI (A-D): (A) In the early phase, the abscess shows concentric enhancement on the post-contrast series. It displays a non-enhancing central necrotic component with (B) central restricted diffusion on ADC. (C) CE-SWI shows a thin ring of peripheral T2* hypointensity. (D) "Ring-like" hypervascularity is seen on DCE. Second MRI (one month later, E-H): (E, H) Once the lesion starts to heal, the central liquefactive component is replaced by granulation tissue and more solid enhancement is observed on the post-contrast series and DCE. (G) A thick T2* hypointense peripheral ring develops on the CE-SWI sequence. (I) A magnified view of CE-SWI demonstrates a well-developed T2* hypointense peripheral ring (red arrowheads). Figure modified from RF Valenzuela, et al. [11].

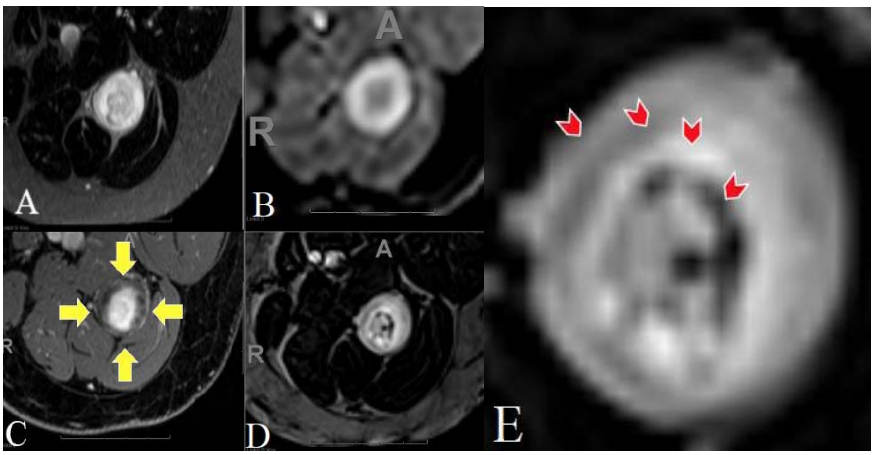

Figure 4: CE-SWI "Target sign" in neurogenic tumors. A sciatic nerve schwannoma in a patient with schwannomatosis is presented. Schwannomas have been associated with the presence of a "target sign" (A). The peripheral myxoid-rich T2 hyperintense layer surrounding the central fibrous region of lower T2 and low (B) ADC signal defines the "target" sign. (C) The "reverse target sign" is demonstrated on this post-contrast axial sequence with delayed central enhancement and peripheral non-enhancement (short yellow arrows). (D) CE-SWI: New patterns emerge with a more complex "onion skin" layered appearance with central areas of low T2* linear and dot-like susceptibility, possibly reflecting slow-flowing veins and fibrous stroma. (E) CE-SWI magnified view of the "onion skin", curvilinear, alternating layers of high and low signal caused by a combination of low T2*, high T2, and T1 shortening imaging effect (red chevrons). This is the CE-SWI "target sign". Figure modified from RF Valenzuela, et al. [11].

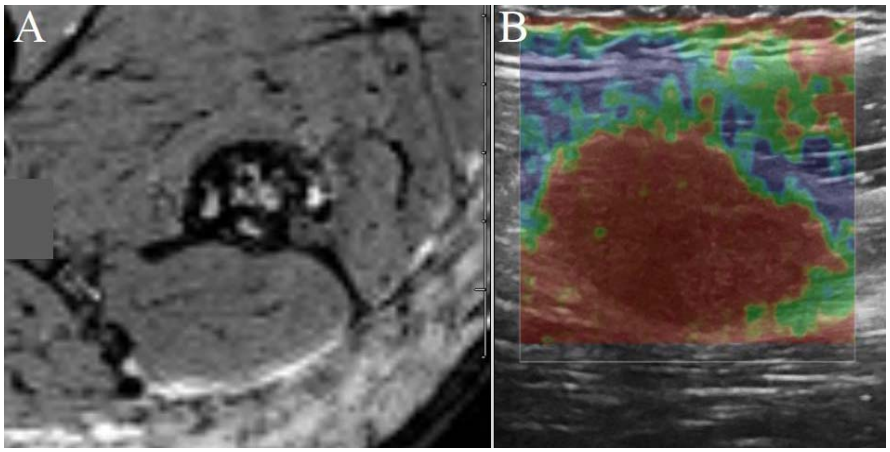

Figure 5: Pathology-proven intramuscular hemangioma of the left thigh: Hemangiomas may show a reproducible linear T2* hypointense signal pattern in the septae and along the capsule on CE-SWI (A). This rather typical appearance likely reflects the presence of fibrous tissue in the septae and capsule, which correlates with increased stiffness on ultrasound elastography (B). Figure modified from RF Valenzuela, et al. [11].

low T2*, high T2, and T1 shortening imaging effects. The observed CE-SWI appearance is a more complex version of the "target sign" typically observed on T2-WI or post-contrast sequences (Figure 4) [36].

CE-SWI in soft-tissue malignant and locally aggressive tumors

Soft tissue sarcoma –CE-SWI has gained notoriety in oncologic MSK imaging because of its sensitivity to blood metabolites in soft tissue lesions, thereby helping to differentiate benign versus malignant soft tissue tumors because many malignant soft tissue tumors demonstrate hemorrhage distributed primarily in the central region of the lesion [23]. Some bone and soft tissue tumor SWI and CE-SWI features have already been described, including giant cell tumors of bone and synovial sarcomas of the soft tissues [24,25]. Hemosiderin T2* hypointense impregnation is seen in both high-grade tumors and benign entities such as pigmented villonodular synovitis and hematomas [26,27]. The pattern of the hemorrhage within soft tissue tumors may be related to biological aggressiveness. Benign tumors are associated with peripheral hemorrhage, while malignant tumors have a central pattern [9]. Among the most common soft-tissue sarcomas, including UPS and LMS, many develop low-grade hemorrhage seen on CE-SWI, which increases in responding tumors during therapy. This phenomenon is often seen simultaneously with decreasing hypervascular components during arterial phase perfusion.

The marked out-of-phase effect of Atypical Lipomatous Tumor (ALT) on CE-SWI is caused by increased cellularity and the co-presence of the fat tissue, causing

linear hypointense areas of signal drop-out that do not represent hemorrhage. The result is a reproducible, rather characteristic pattern that we describe as a "feathery appearance" (Figure 6). The signal pattern of CE-SWI increases specificity for distinguishing between simple lipomas and more cellular low-grade lipomatous tumors such as ALT.

On CE-SWI, most of the myxoid sarcomas demonstrate absent or just low-grade intratumoral hemorrhage on the baseline pre-treatment exam. CE-SWI often demonstrates a high degree of T1 shortening with T2 hypointense septae and venous structures in sarcomas with abundant myxoid components. Low-grade liposarcomas/adipocytic sarcomas may demonstrate a prominent out-of-phase effect caused by highly cellular atypical fat that is not detectable by the T1 sequence. In myxoid liposarcomas, where mature or atypical fat is relatively minimal and myxoid components are the predominant tissue element, CE-SWI demonstrates a high T1 shortening in enhancing tissue, with internal T2 hypointense septae and venules. Such venular structures are no longer recognizable after baseline following treatment with systemic cytotoxic therapy, while ADC_{mean} rises, and arterial perfusion diminishes in an otherwise stable-sized mass [11,30].

Desmoid fibromatoses: Although T2-WI imaging is generally considered the gold standard for desmoid tumor response assessment, CE-SWI demonstrates superb discrimination between muscle vs. mature collagenized tumor vs. immature enhancing tumor suggesting its high value in the assessment of desmoid tumor treatment and surveillance. CE-SWI-based volumetric and mChoi measurements could improve the prediction of response/progression in desmoid tumors by providing a better assessment with 3D tumor size measurements. It could enhance the discrimination between the mature collagenized and immature enhancing components, that predominate in mature responsive and immature progressive disease, respectively (Figure 7). The use of CE-SWI as a single MRI sequence can provide insight regarding the underlying biological changes of responsive and progressive desmoid tumors using 3D volumetric assessment, allowing improved separation of T2-hypointense mature collagenized tumor from T2-hyperintense, T1-shortened-enhancing, immature or progressive tumor components [40].

Soft-tissue sarcoma treatment response

Response Evaluation Criteria in Solid Tumors (RECIST) has limited applicability because sarcomas typically demonstrate many more relevant therapeutic changes than size alone. As a result of therapy, sarcomas typically demonstrate many changes in composition, such as hemosiderin deposition and granulation tissue formation, fibrosis, inflammation, and calcification. These changes should be considered in the estimation of tumor response. SWI can help to assess treatment response in these lesions because the pattern of internal bleeding can change in recognizable ways due to therapy-induced necrosis (TIN) in responding tumors [31]. Post-hemorrhagic hemosiderin deposition assessment can be performed with CE-SWI as a "NON-RECIST" treatment response indicator. Learning and understanding the hemorrhage patterns that occur spontaneously in high-grade sarcomas as part of their natural progression while differentiating them from those occurring as part of the therapy-induced necrosis process in responding to tumors has yet to be fully assessed [27]. At our institution, we have

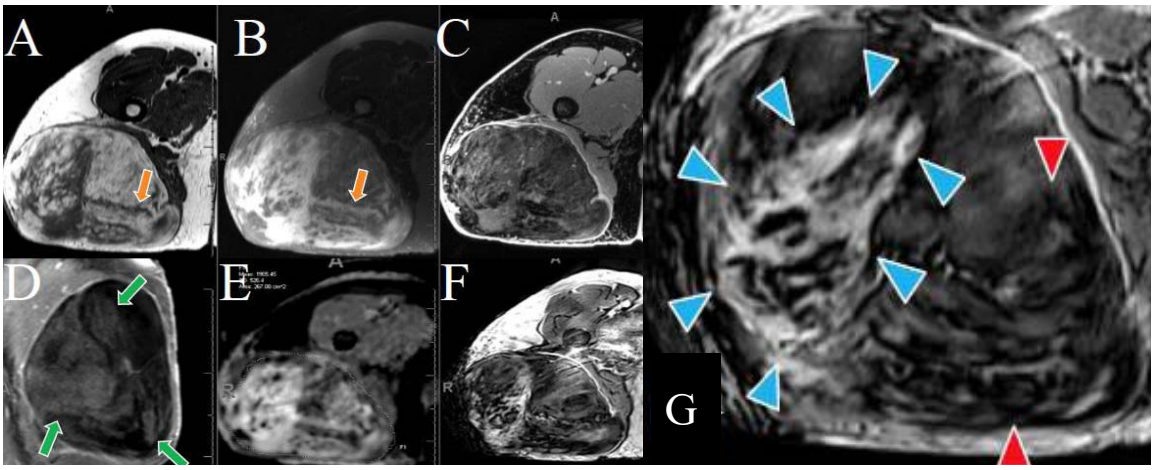

Figure 6: Well-differentiated liposarcoma with myxoid content arising from the right thigh. (A) T1-WI axial imaging demonstrates a T1 hyperintense lipomatous mass with linear T1 hypointense septae (orange arrow). (B) Axial T2-WI shows hyperintense internal septae (orange arrows). (C) Axial post-contrast imaging (Dixon-water) shows linear capsule-like enhancement without clear nodularity. (D) Sagittal dynamic perfusion PWI/DCE shows hazy/cloud-like delayed wash-in without hypervascular nodular components (green arrows). (E) DWI and ADC maps show increased signals along the T2 hyperintense septae. The whole-tumor ADC mean is 1.9 x 10-3 mm2/s. Counterintuitively, high ADC values are often seen in malignant myxoid tumors. (G) CE-SWI displays T1-shortening more prominently than the areas of enhancement on the post-contrast Dixon-water sequence (blue arrowheads, compared with Figure C). T2 hypointense septae are also present. Figure modified from RF Valenzuela, et al. [11].

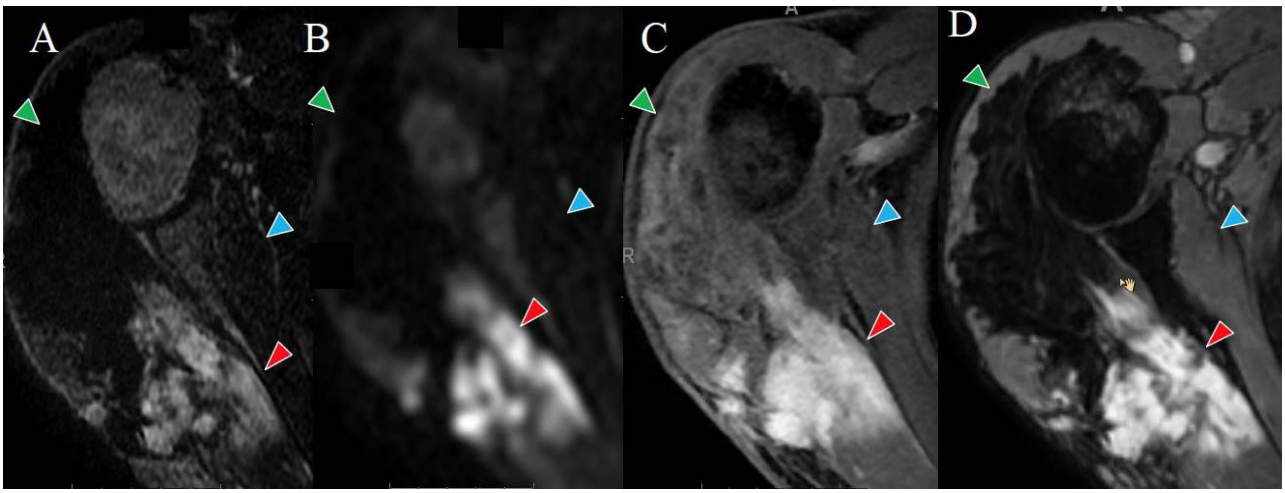

Figure 7: Desmoid Fibromatosis of the right shoulder. (A) Axial T2W short-tau inversion recovery (STIR) demonstrates the hypointensity of the mature collagenized components (green arrowheads) and the hyperintensity of the immature elements (red arrowheads). (B) Axial DWI b800 shows hyperintense immature components (red arrowheads) due to increased cellularity. (C) Axial Dixon-water post-contrast shows poor discrimination between mature (collagenized) tumor components (green arrowhead) and normal muscle (blue arrowhead). (D) and CE-SWI demonstrates a higher degree of tissue separation between the normal muscle (blue arrowheads), the mature (collagenized) tumor components (green arrowheads), and the immature (cellular) tumor elements (red arrowheads). Figure modified from RF Valenzuela, et al. [11].

initially explored CE-SWI, where susceptibility (T2*) and T1 shortening are combined in contrast-enhanced SWI sequences, demonstrating highly promising results. In soft tissue tumors, this sequence can also display the viable, enhancing portions of a soft tissue sarcoma separately from hemorrhagic/necrotic components, suggesting its utility for evaluating tumor treatment response [13,26]. During successful systemic therapy, CE-SWI demonstrates an initial "interstitial" or "globular" pattern of hemorrhage. After three months of successful therapy, a central or "luminal" pattern emerges, and after four months, a "wall impregnation" pattern can be seen (Figure 8). In an institutional UPS series, the "complete ring" of hemosiderin was most commonly observed in tumors with more than 90% treatment induced necrosis at the presurgical MRI, while in tumors with treatment-induced necrosis, only between 31-89% were most associated with an "incomplete ring" of hemosiderin. Non-responders with less than 30% necrosis often displayed a "globular" hemorrhage pattern after treatment [11,12,30] (Figure 9). Diffusion-weighted Imaging (DWI) ADC maps may show a paradoxical decrease in ADC due to hemorrhage T2*/susceptibility effect unrelated to increased cellularity (Figure 10). Necrosis products such as protein hemosiderin and methemoglobin can also falsely lower ADC values.

CE-SWI in post-surgical soft tissues

Post-surgical seromas with and without associated hemorrhage have a wide range of appearances depending on their degree of protein and hemorrhagic content. Hemosiderin and methemoglobin content tend to create dependent T2* hypointense layering (Figure 11). At the same time, the fibrous capsule of the surgical cavity demonstrates linear enhancement and T2* hypo intensity, along with numerous micro-susceptibility wall artifacts caused by the cauterization of the surgical walls (Figure 12). The capsule appearance caused by a combination fibrotic tissue, hemosiderin impregnation, or both. CE-SWI demonstrates a greater internal signal complexity caused by signal arising from protein-rich serum and methemoglobin layering.

Myocutaneous flaps: Radical tumor resection often requires soft-tissue reconstruction via the use of myocutaneous flap reconstruction. The appearance of the flaps may occasionally overlap with the tumor. On CE-SWI, a reproducible pattern emerges, where the intermuscular fat layers become dark due to an out-of-phase/chemical shift effect at the interface with the muscle layers. This creates alternating hyper and hypointense layers responsible for the "layered cake" appearance. This pattern resembles the appearance previously described in reconstructive orthopedic surgery and is based on T1 sequences [40]. It can help differentiate a normal flap from infiltrative tumors such as recurrent myxoid sarcomas, which do not typically demonstrate such a layered appearance (Figure 13).

Soft-tissue sarcoma recurrence

Early recurrence of myxoid sarcomas is, in our experience, particularly difficult to diagnose as their high DWI/ADC and T2 signal and enhancement pattern may mimic benign postoperative granulation tissue. The demonstration of hypervascular enhancing nodules on PWI may represent a useful sign for the early detection of recurrent myxoid sarcomas. CE-SWI can demonstrate both the standard T2* susceptibility that is typical of post-surgical findings combined with T1 shortening in areas of nodular enhancement (Figure 14) [11,30].

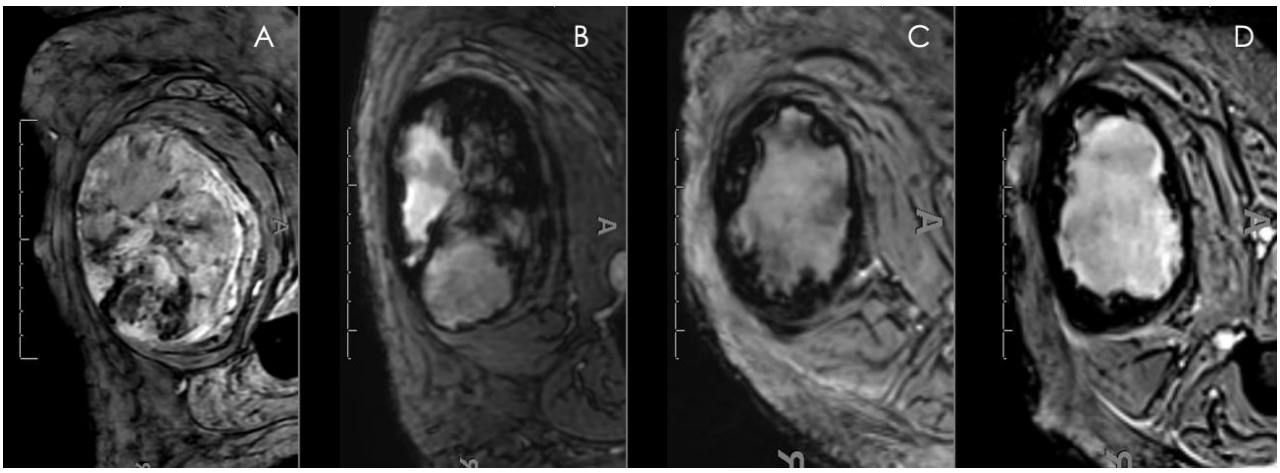

Figure 8: UPS CE-SWI therapy-induced changes in responders: Hemorrhage as a biomarker of response. CE-SWI from left to right thigh demonstrating a UPS at different stages during therapy: A, Baseline; B, post-chemo Cycle 1; C, post-chemo last cycle; and D, post-radiation (PRT). There was 99% necrosis on the histologic specimen. The images demonstrate the development of the Complete Ring pattern. Figure modified from Valenzuela, R. F., Amini B, Duran-Sierra E, Canjirathinkal MA, Madewell JE, Costelloe CM, Murphy WA. Multiparametric MRI for the Assessment of Treatment Effect and Tumor Recurrence in Soft-tissue Sarcoma of the Extremities. Journal of Radiology and Oncology. 2023; 7(3): 058-065.

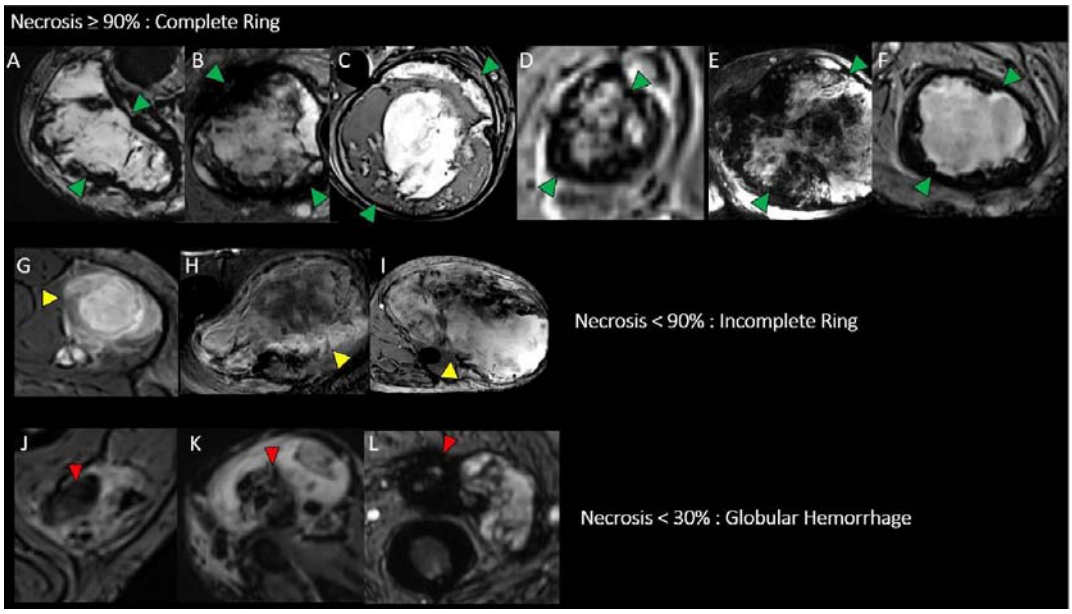

Figure 9: SWI: Hemorrhage as a biomarker of response in Undifferentiated Pleomorphic Sarcoma (UPS): (A-F) Six UPS cases demonstrating a T2* hypointense "complete ring-like" CE-SWI pattern (green arrowheads). This is caused by hemosiderin and the deposition of fibrous tissue in successfully treated sarcomas with more than 90% of treatment-induced necrosis. (G-I) Three UPS cases with TIN in the 30% - 89% range tend to demonstrate an "incomplete ring-like" T2* hypointense pattern (yellow arrowheads pointing to areas of segmental ring absence). (J-L) Four UPS cases with less than 30% TIN showed a" globular" T2* hypointense pattern (red arrowheads). Figure modified from RF Valenzuela, et al. [11].

CE-SWI in primary benign bone tumors

Benign primary bone tumors – SWI and CE-SWI have limited value in evaluating marrow trabeculae and chondroid matrix due to artifacts caused by the multiple tissue interfaces. These structures are predominately hypointense on magnitude images [9]. Bender, et al. (2017) studied 56 vertebral hemangiomas with SWI and conventional MRI (T1 and T2), using conventional MRI, radiographs, and CT as the reference standard. When SWI was added to conventional MRI, all lesions were identified without needing x-ray-based imaging modalities (15). Brown tumors are reactive bone lesions that contain large amounts of hemosiderin due to repetitive microtrauma and can demonstrate a marked susceptibility effect on T2* gradient echo imaging. This appearance can help narrow the differential diagnosis of lytic lesions in patients with hyperparathyroidism [38]. Other lytic lesions that typically contain hemosiderin include pigmented villonodular synovitis, giant cell tumors (Figure 15), giant cell reparative granulomas, hemorrhagic bone cysts (Figure 16), and pseudotumor of hemophilia [39].

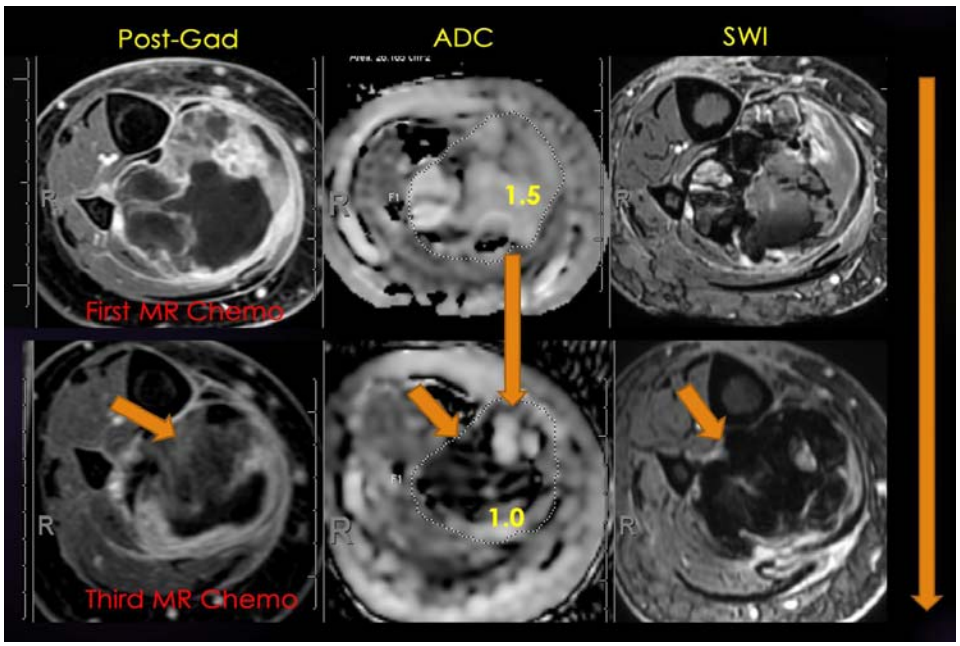

Figure 10: Soft tissue leiomyosarcoma (LMS) displaying a response to cytotoxic chemotherapy with the development of hemorrhage and decreased arterial perfusion. Because of the blood products, a paradoxical decrease in ADC is seen in the responding tumor. The initial SWI pattern after a month of therapy is an "interstitial: pattern. After three months a central or "luminal" pattern emerges and after four months a "wall impregnation" pattern is evident.

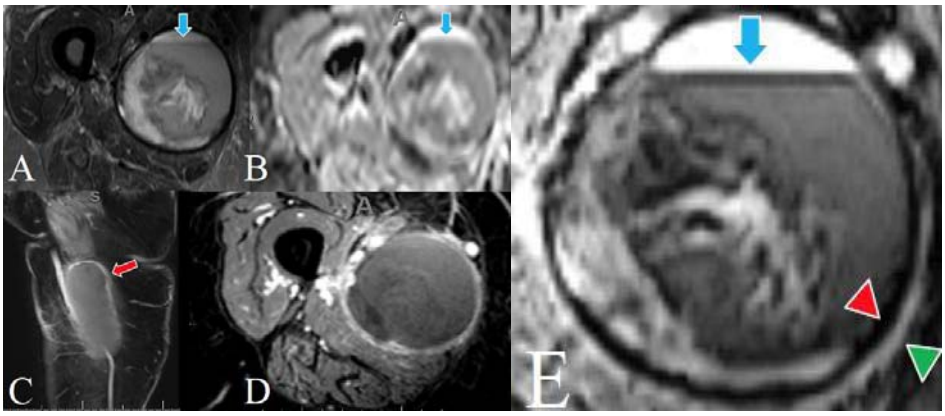

Figure 11: CE-SWI appearance of post-surgical seromas: (A) T2W imaging shows a T2 hypointense capsule and complex internal layering (blue arrows). (B) Findings on the ADC map are like those seen in T2W imaging. (C) Dynamic PWI/DCE demonstrates low-grade delayed capsular enhancement (red arrow) without nodular hypervascular components. (D) The post-contrast sequence shows an enhancing ring like on PWI/DCE. (E) CE-SWI demonstrates ring-like T1 shortening in the outermost layer of the seroma capsule (green arrowhead), with a ring of T2* hypointensity along the inner capsule (red arrowhead). This CE-SWI "double ring" sign is commonly seen in hemorrhagic seromas. Figure modified from RF Valenzuela, et al. [11].

In Giant Cell Tumors, the observed CE-SWI **"honeycomb-like"** appearance corresponds with the underlying tumor architecture, including numerous cystic blood-filled spaces. The deep T2* hypo intensity foci arise from hemosiderin layering areas. This appearance may help recognize GCT.

In Unicameral Bone Cysts (UBC) CE-SWI, the blood products demonstrate T2* hypointensity in the dependent position, with accentuated detail of the internal septae, typically obscured in all other sequences.

CE-SWI in malignant bone tumors and metastases

Chondrosarcomas tend to be T2 hyperintense expansile lesions that are not typically hypervascular nor diffusion restricting on ADC. The "ring and arcs" of chondroid matrix mineralization, commonly recognized on CT, are seen on CE-SWI as ring-like areas of T2* susceptibility within the lesion (Figure 17). On tumor-infiltrated bone, CE-SWI can often demonstrate underlying residual trabecular bone structure that is not perceptible on conventional MRI (Figures 17,18). CE-SWI is a technique that can help map primary and metastatic bone lesions by differentiating between T1-shortening/enhancing tumors and normal iron-loaded T2* hypointense normal bone marrow (Figure 19). In hypervascular metastases, CE-SWI can show a complex pattern, including diffuse T1 shortening/

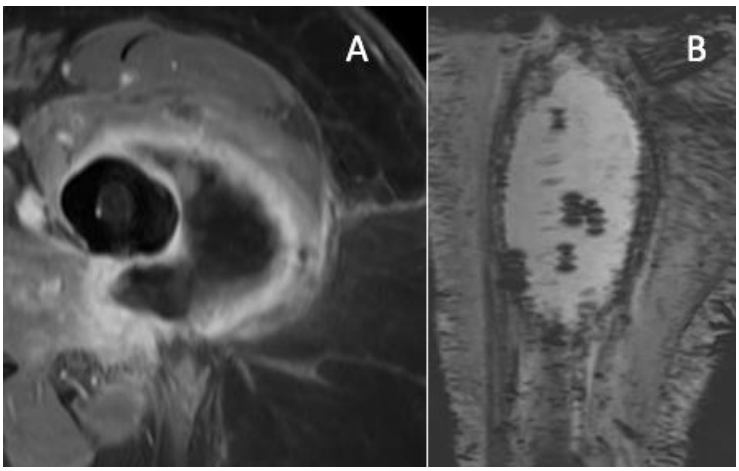

Figure 12: CE-SWI appearance of post-surgical seromas: (A) The post-contrast sequence shows ring-like enhancement (B) CE-SWI demonstrates a T2* hypointense surgical cavity with a fibrous capsule, along with numerous micro-susceptibility wall artifacts caused by the cauterization of the surgical walls.

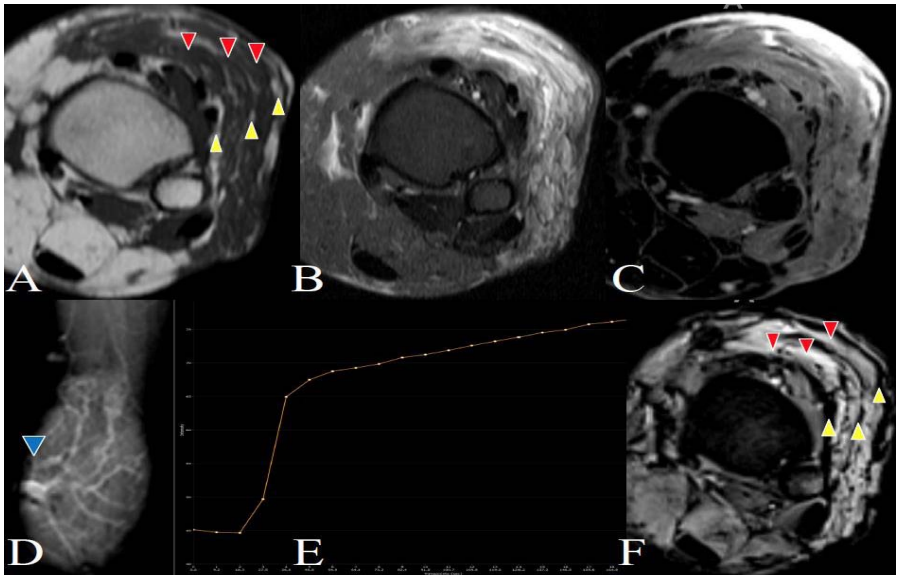

Figure 13: Myocutaneous flaps are often used to reconstruct surgical sites after radical resection of soft-tissue sarcomas of the extremities. (A) T1W axial images typically demonstrate a pattern of T1 hyperintense fascicular fat (yellow arrowheads in A, F) separating layers of muscle (red arrowheads in A, F). Such a separation of tissues is not as well appreciated in fat-suppressed T2W imaging (B) or fat-suppressed post-contrast sequences (C). (D and E) It is often easy to identify a vascular pedicle (blue arrowhead) irrigating the entire flap on DCE perfusion. A kinetic TIC (time-intensity curve) type V is often seen across the flap. (F) On CE-SWI, a reproducible pattern emerges, where the fat layers become dark due to an out-of-phase/chemical shift effect at the interface with the muscle layers. This creates alternating hyper and hypointense layers responsible for the "layered cake" appearance. Figure modified from RF Valenzuela, et al. [11].

contrast enhancement and multifocal and serpiginous T2* hypo intense foci. These foci likely represent prominent neovascularity (Figure 20).

Utilizing the capabilities of the filtered phase images to recognize calcium may lead to reliable differentiation between osteoblastic and osteolytic spine metastases with an accuracy superior to the standard spine MRI sequences [3]. CE-SWI can discriminate normal from metastatic or primary tumor-replaced bone marrow. This can be achieved by the high sensitivity of CE-SWI to the T2* blooming effect arising from healthy iron-loaded bone marrow as opposed to the T1-shortening caused by the tumor infiltration of the marrow (Figure 19). Occasionally in hypervascular metastases, multifocal and serpiginous T2* hypointense foci likely representing prominent neovascularity can be observed on CE-SWI (Figure 19) [11].

SWI and CE-SWI in articular pathology

Erosions in arthritis - Calcium is diamagnetic and produces a negative phase shift, allowing evaluation by SWI. Ulas, et al. (2019) demonstrated that SWI could detect the decreased calcium density corresponding to bone erosions in patients with hand arthropathies. SWI is superior to sequences such

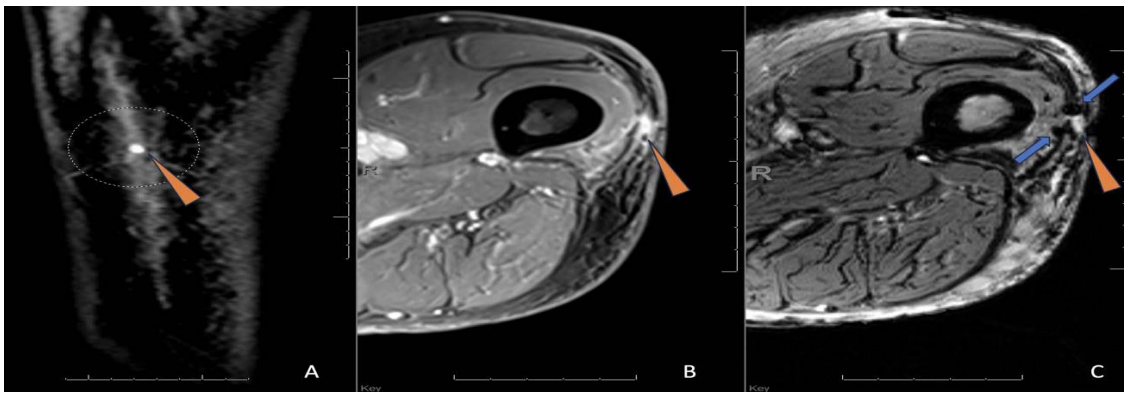

Figure 14: Early recurrence of myxofibrosarcoma. (A) The sagittal dynamic post-contrast sequence (DCE) shows nodular hyper vascular enhancement (orange arrowhead). (B) The axial post-contrast sequence demonstrates nodular soft-tissue enhancement (orange arrowhead) (C) CE-SWI demonstrates a T2* hypointense surgical micro-susceptibility artifacts (blue arrows) surrounding an enhancing soft-tissue nodule (orange arrowhead) (sentinel artifact).

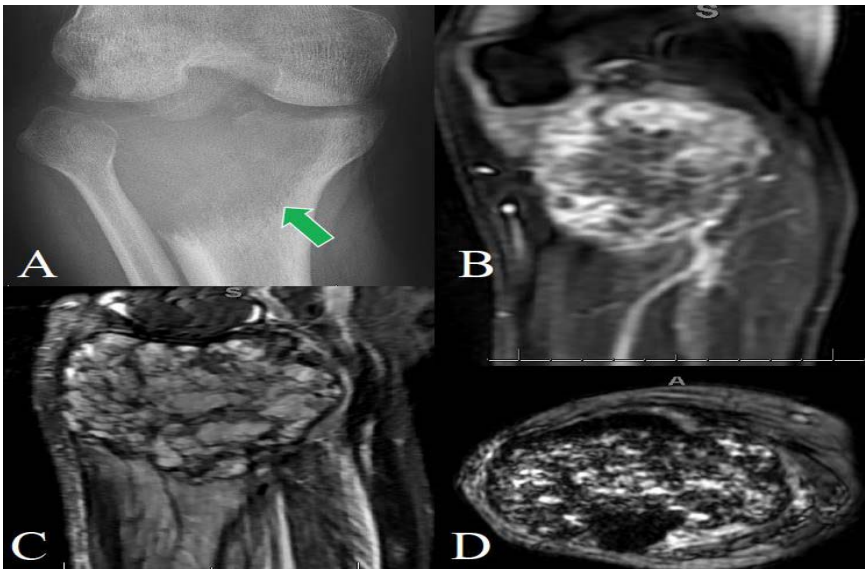

Figure 15: Giant cell tumor of bone (GCT) arising from the proximal tibia. Although considered benign, these tumors can be locally aggressive. (A) This tumor demonstrates a lytic, destructive appearance and an ill-defined zone of transition (green arrow) with absent peripheral sclerosis, as seen on the PA radiograph of the knee. (B) Aggressive osteolysis often correlates with hypervascularity on PWI/DCE imaging. (C) GCT has a dense "honeycomb-like" septal mesh pattern with multifocal fluid-fluid levels, as is typically described on T2W imaging. (D) CE-SWI amplifies these effects. Figure modified from RF Valenzuela, et al. [11].

as VIBE, where the T2* effect produced by calcium results in signal loss. SWI uses this property to produce useful signal changes [19].

PVNS/TGCT and Hemophilic arthropathy: Synovial proliferation and hemosiderin impregnation are usual features in Pigmented Villonodular Synovitis (PVNS)/ Tenosynovial Giant Cell Tumors (TGCT) (Figures 21,22). Gradient-echo imaging also has been described with enhanced imaging as useful in diagnosing and assessing the extent of PVNS in pediatric patients [42], in which low signal mass behind the cruciate ligaments may represent an important diagnostic feature. Similarly, CE-SWI will demonstrate T2* blooming in the affected tendon or joint (Figures 21,22). Similar findings, often associated with joint destruction, are observed in hemophilic arthropathy [11] (Figure 20). Hemophilic arthropathy and PVNS are part of the differential diagnosis of T2* hypointense CE-SWI synovial proliferation.

Conclusion

CE-SWI is a promising imaging technique for the characterization of oncologic musculoskeletal (MSK) conditions. It is highly sensitive to blood products and can identify soft-tissue calcifications and collagenization. Compared to traditional T2W imaging, CE-SWI provides better differentiation between mature fibrotic T2* dark components and active enhancing elements in desmoid fibromatosis.

CE-SWI can also demonstrate the viable enhancement of portions of soft tissue sarcoma separately from hemorrhagic/

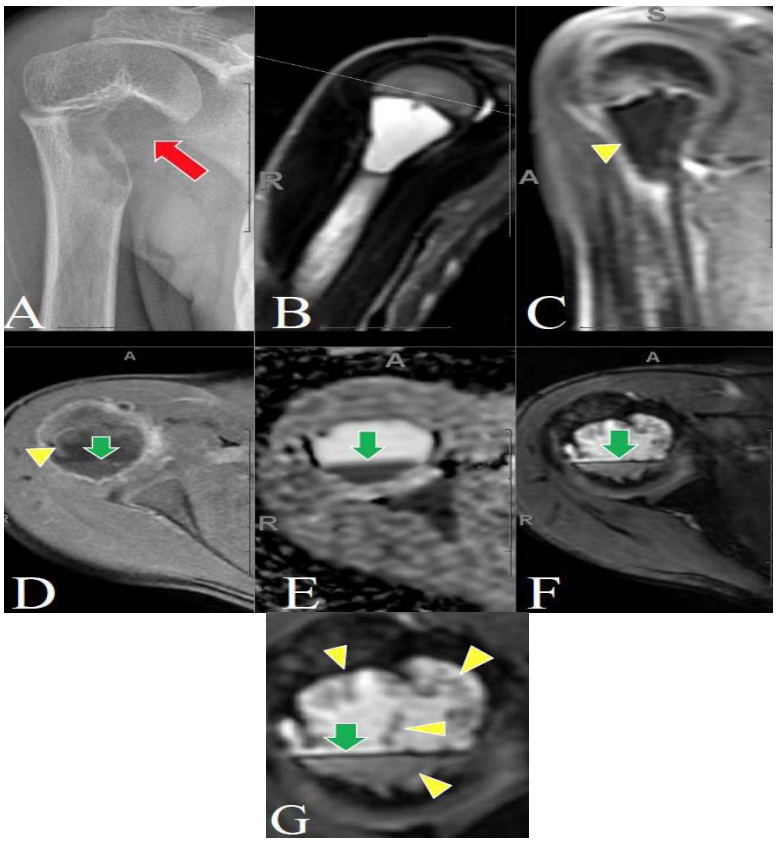

Figure 16: Unicameral bone cyst (UBC) of the proximal right humerus. (A) A radiograph of the lateral humerus shows a lucent lesion with cortical destruction. (B) UBC tends to demonstrate a homogenous high signal on T2W imaging, as seen in the coronal T2 sequence. (C, D) UBC tends to show linear peripheral enhancement, as seen on PWI/DCE (yellow arrowhead) and post-contrast sequences. On standard sequences, the dependent layering of blood products can be seen (green arrows). This effect is maximized on (E) ADC and (F) CE-SWI, where the blood products demonstrate T2* hypointensity in the dependent position. (G) Magnified CE-SWI indicates in detail the internal septae (yellow arrowheads) that are completely obscured in all other sequences. Figure modified from RF Valenzuela, et al. [11].

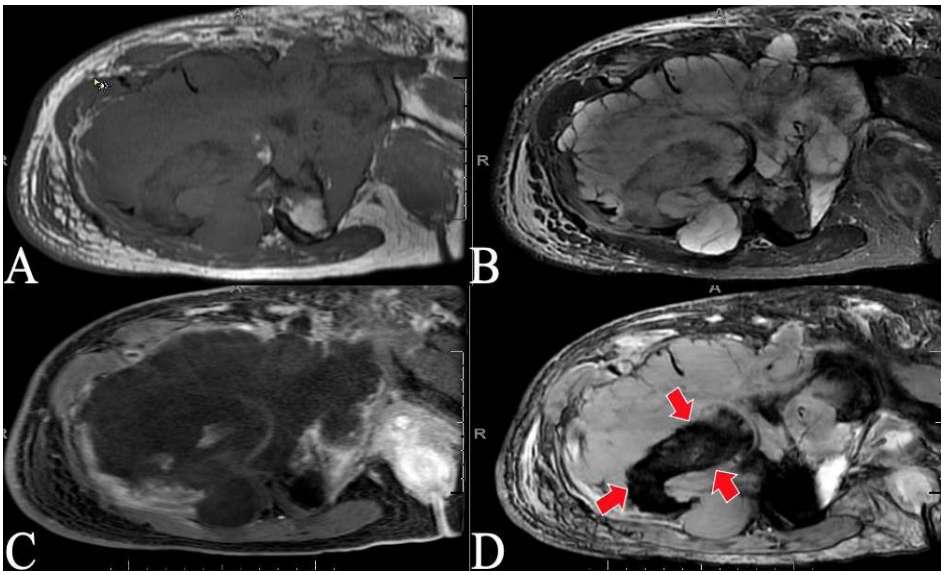

Figure 17: Chondrosarcoma infiltrating the right hemipelvis and hip. (A) The tumor demonstrates intermediate T1 and (B) high T2 signals across the bone and soft-tissue components. (C) On the post-contrast sequence, the tumor demonstrates low-grade peripheral enhancement. (D) On CE-SWI, the tumor shows an intermediate-high signal across the soft-tissue components. A unique feature of bone evaluation on CE-SWI is that it can accentuate the persistence of the infiltrated bone's trabecular structure (red arrows), which can otherwise appear destroyed on conventional sequences. This phenomenon is caused by the predominantly T2* hypointense trabeculae and iron-loaded bone marrow susceptibility effect. Figure modified from RF Valenzuela, et al. [11].

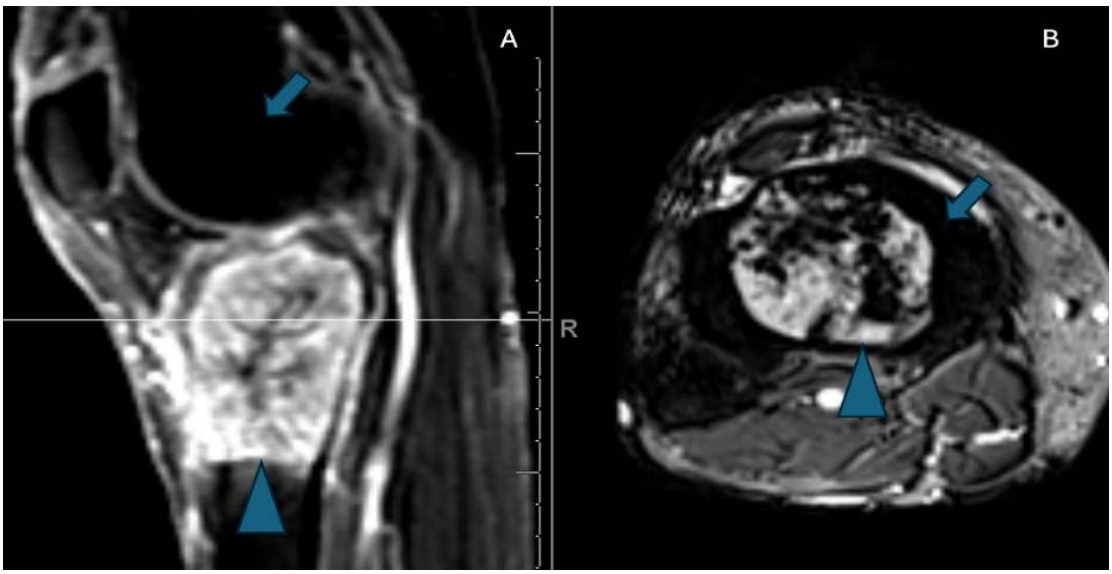

Figure 18: Metastatic renal cell carcinoma (RCC) to the tibia. (A) Sagittal PWI/DCE demonstrated hyper vascular enhancing metastatic lesion in the proximal tibia (arrowhead). (B) T2* shortening within the healthy iron-loaded red bone marrow (arrow) with enhancement of metastatic RCC (arrowhead).

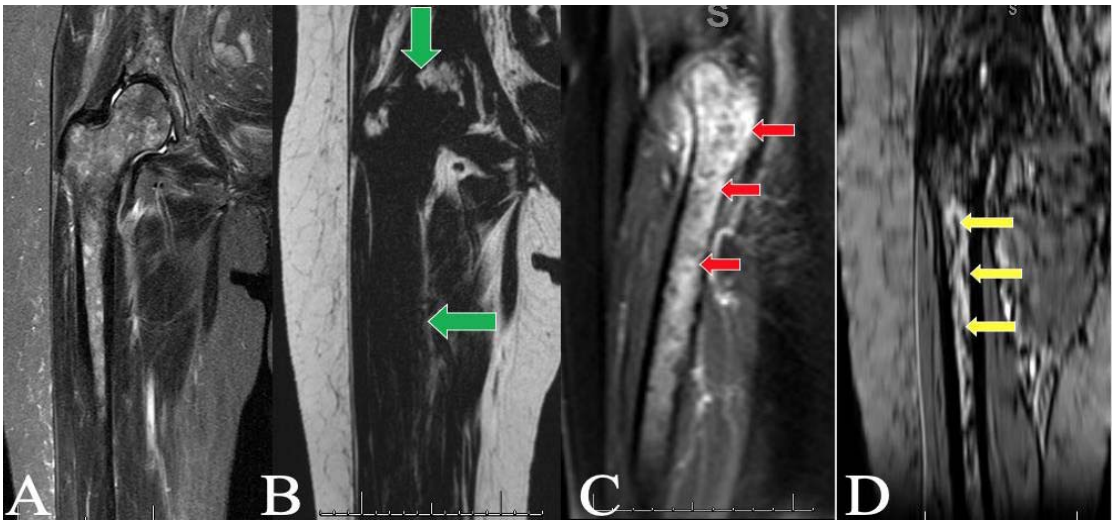

Figure 19: Hypervascular bone metastases in the right femur of a breast cancer patient with mixed lobular and ductal breast carcinoma. (A) T2W coronal STIR sequence, demonstrating diffusely heterogenous bone marrow tumor infiltration. (B) Coronal Dixon-fat-only sequence showing complete replacement of normal fat-containing marrow (green arrows). (C) Sagittal PWI/DCE demonstrates diffusely infiltrating hypervascular tumor with a serpiginous pattern (red arrows). CE-SWI(D) coronal reconstruction shows a complex pattern. This includes diffuse T1 shortening due to contrast enhancement and multifocal and serpiginous T2* hypo intense foci (yellow arrows), likely representing prominent neovascularity. Figure modified from RF Valenzuela, et al. [11].

necrotic components, thus serving as a biomarker of tumor grade and treatment response. It is important to differentiate between the hemorrhage patterns that occur spontaneously in high-grade sarcomas and those that arise in treatment-induced necrosis. CE-SWI can provide insight into the treatment response assessment in responding tumors. In successfully treated sarcomas, a ring-like hemosiderin CE-SWI pattern is often observed.

Moreover, CE-SWI can differentiate between normal and tumor-replaced bone marrow. It is sensitive to the T2* blooming effect caused by healthy iron-loaded bone marrow as opposed to the T1-shortening caused by the tumor.

CE-SWI is a potentially powerful imaging tool for analyzing several MSK oncologic pathologies. It is already considered an integral part of our institutional multiparametric oncologic baseline and treatment MRI evaluation. CE-SWI is available on commercial MRI scanners and can be used at other institutions as part of the MRI MSK sequence armamentarium.

In summary, CE-SWI's most important MSK oncology applications include:

To demonstrate soft-tissue and bone calcifications

To discriminate between mature fibrotic T2* dark

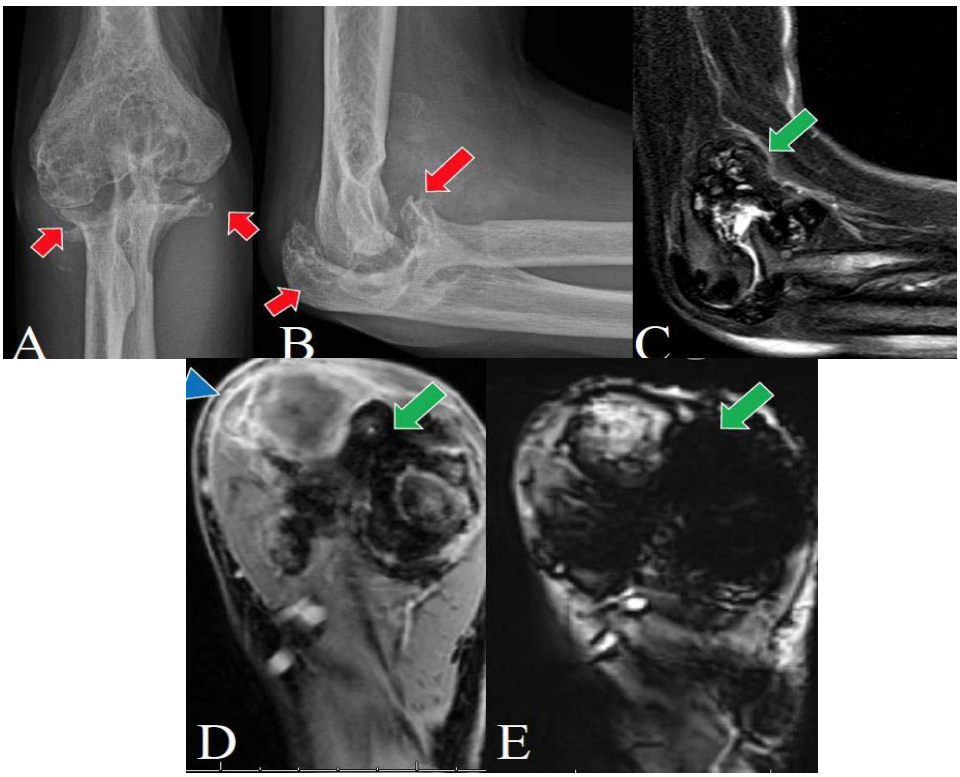

Figure 20: Articular disease hemophilic elbow: Joint overgrowth, destruction, synovial proliferation, and hemosiderin impregnation are usual features of hemophilic arthropathy. (A and B) AP and lateral radiographs of the right elbow demonstrate articular destruction and bone overgrowth (red arrows). (C) Sagittal T2W image demonstrates deeply hypointense nodular synovial proliferation (green arrow). (D) The axial post-contrast sequence demonstrates rim-like peripheral synovial enhancement (blue arrowhead). (E) CE-SWI demonstrates deep T2* hypo intensity across the hemosiderin-impregnated synovium (green arrow). Figure modified from RF Valenzuela, et al. [11].

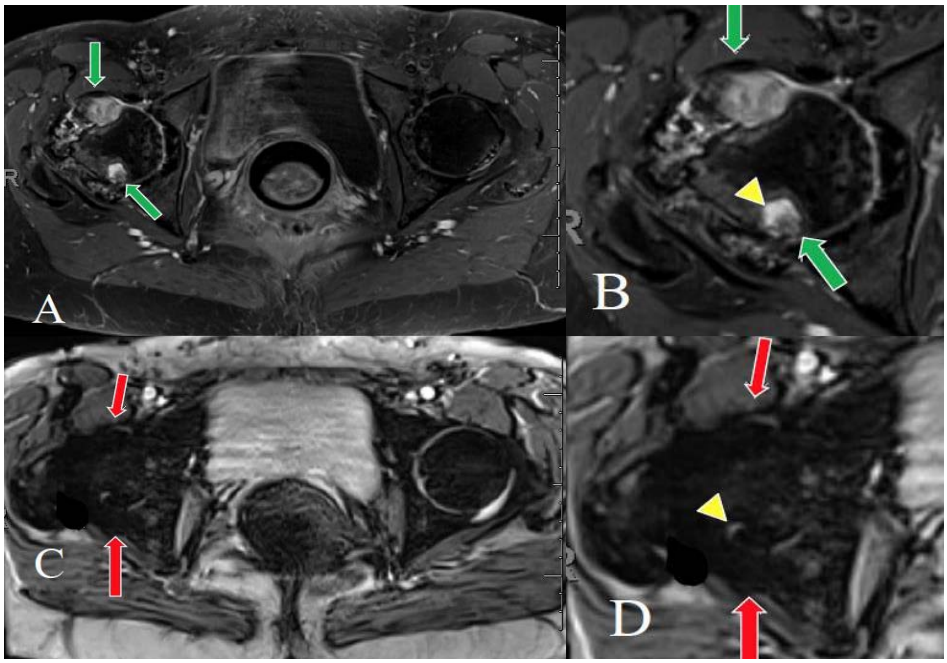

Figure 21: PVNS with articular erosions: (A and B) Post-contrast axial imaging using a Dixon-water sequence demonstrates nodular areas of T1 shortening (green arrows) associated with erosions of the right femoral head and neck. (C and D) CE-SWI demonstrates hemosiderin-impregnated synovium with deep T2* hypointensity and blooming (red arrows). Other areas of synovial proliferation demonstrate lesser degrees of hemosiderin impregnation. These areas undergo T1-shortening following intravenous contrast administration, but the contrast enhancement can be obscured by prominent T2* blooming (yellow arrowhead). This effect is a common pitfall of CE-SWI concerning the areas of synovial proliferation in PVNS. Figure modified from RF Valenzuela, et al. [11].

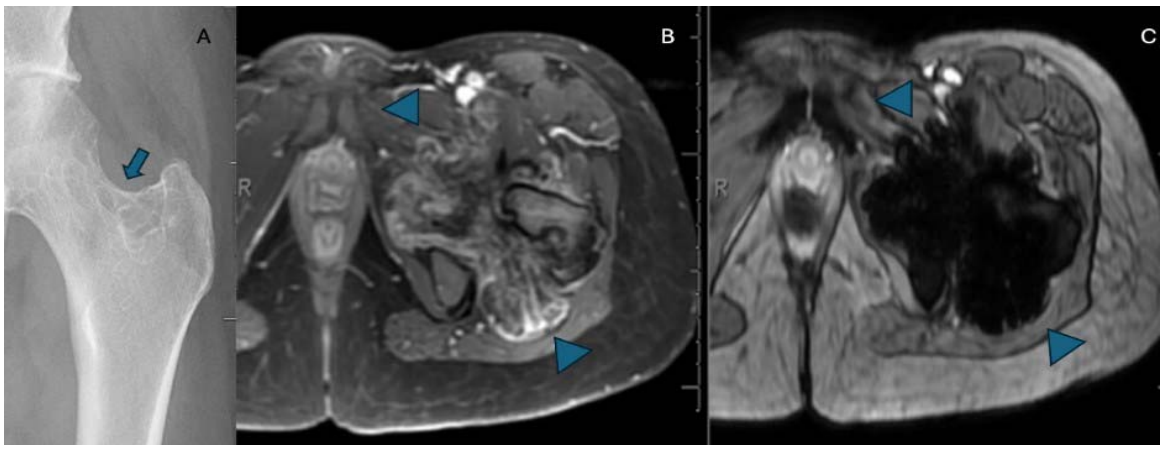

Figure 22: PVNS of the left hip. (A) AP radiograph of the left hip demonstrates bone remodeling and erosions (arrow). (B) Axial FS T1W imaging post gadolinium contrast shows mild heterogeneous enhancement of a mass-like synovial proliferation arising from the left hip joint with T1 shortening and mild hyperintensity to the muscle (arrowheads). (C) Axial CE-SWI sequence demonstrates extensive T2* shortening/susceptibility. Areas of T2* hypointensity represent synovial proliferation hemosiderin impregnation (arrowheads).

components and active enhancing elements in desmoid fibromatosis.

To demonstrate T2* morphologic patterns associated with Soft-Tissue Sarcoma treatment response.

To discriminate normal from tumor-replaced bone marrow.

To demonstrate T2* hypointense hemosiderin impregnated PVNS and GCT.

Acknowledgment

The John S. Dunn, Sr. Distinguished Chair in Diagnostic Imaging.

M.R. Evelyn Hudson Foundation Endowed Professorship.

References

1. Haacke EM, Xu Y, Cheng YC, Reichenbach JR. Susceptibility weighted imaging (SWI). Magn Reson Med. 2004 Sep;52(3):612-8. doi: 10.1002/mrm.20198. PMID: 15334582.
2. Haacke EM, Mittal S, Wu Z, Neelavalli J, Cheng YC. Susceptibility-weighted imaging: technical aspects and clinical applications, part 1. AJNR Am J Neuroradiol. 2009 Jan;30(1):19-30. doi: 10.3174/ajnr.A1400. Epub 2008 Nov 27. PMID: 19039041; PMCID: PMC3805391.
3. Böker SM, Adams LC, Bender YY, Fahlenkamp UL, Wagner M, Hamm B, Makowski MR. Differentiation of Predominantly Osteoblastic and Osteolytic Spine Metastases by Using Susceptibility-weighted MRI. Radiology. 2019 Jan;290(1):146-154. doi: 10.1148/radiol.2018172727. Epub 2018 Oct 30. PMID: 30375926.
4. Rauscher A, Sedlacik J, Barth M, Mentzel HJ, Reichenbach JR. Magnetic susceptibility-weighted MR phase imaging of the human brain. AJNR Am J Neuroradiol. 2005; 26: 736-742. [PMID:15814914]
5. Yamada N, Imakita S, Sakuma T, Takamiya M. Intracranial calcification on gradient-echo phase image: depiction of diamagnetic susceptibility. Radiology. 1996; 198: 171-178. [PMID: 8539373 DOI: 10.1148/radiology.198.1.8539373]
6. Halefoglu AM, Yousem DM. Susceptibility weighted imaging: Clinical applications and future directions. World J Radiol. 2018 Apr 28;10(4):30-45. doi: 10.4329/wjr.v10.i4.30. PMID: 29849962; PMCID: PMC5971274.
7. Sood S, Gupta R, Modi J, Sharma J. Susceptibility Weighted Imaging: Physics and Clinical Applications in Neuroimaging at 3 Tesla. European Congress of Radiology - ECR 2014. 2014. https://epos.myesr.org/poster/esr/ecr2014/C-1472
8. Wu Z, Mittal S, Kish K, Yu Y, Hu J, Haacke EM. Identification of calcification with MRI using susceptibility-weighted imaging: a case study. J Magn Reson Imaging. 2009 Jan;29(1):177-82. doi: 10.1002/jmri.21617. PMID: 19097156; PMCID: PMC2646180.
9. Martín-Noguerol T, Montesinos P, Casado-Verdugo OL, Beltrán LS, Luna A. Susceptibility Weighted Imaging for evaluation of musculoskeletal lesions. Eur J Radiol. 2021 May;138:109611. doi: 10.1016/j.ejrad.2021.109611. Epub 2021 Feb 28. PMID: 33677418.
10. Barbosa JH, Santos AC, Salmon CE. Susceptibility weighted imaging: differentiating between calcification and hemosiderin. Radiol Bras. 2015 Mar-Apr;48(2):93-100. doi: 10.1590/0100-3984.2014.0010. PMID: 25987750; PMCID: PMC4433298.
11. Valenzuela RF, Amini B, Duran-Sierra E, Canjirathinkal M, Idrees H, Madewell J, Costelloe C, Murphy W. Susceptibility-Weighted Imaging (SWI) in Benign and Malignant Tumors of the Musculoskeletal System. 2023. https://dx.doi.org/10.26044/ecr2023/C-19005
12. Sierra DRF, Valenzuela M, Canjirathinkal J, Madewell W, Murphy C, Amini CB. Susceptibility Imaging (SWI) Morphologic Patterns and High-Order Radiomics of Baseline and Post-Treatment Advanced MRI of Extremity Soft Tissue Undifferentiated Pleomorphic Sarcoma.2023. https://dx.doi.org/10.26044/ecr2023/C-19060
13. Jie L, Yong C, Xuemei B. Study of susceptibility-weighted imaging on MR and pathologic findings to distinguish benign or malignant soft tissue tumor. Chin J Oncol. 2017; 39(5).
14. Takeuchi M, Matsuzaki K, Harada M. Clinical utility of susceptibility-weighted MR sequence for the evaluation of uterine sarcomas. Clin Imaging.2019Jan-Feb;53:143-150.doi:10.1016/j.clinimag.2018.10.015. Epub 2018 Oct 13. PMID: 30340078.
15. Nörenberg D, Ebersberger HU, Walter T, Ockert B, Knobloch G, Diederichs G, Hamm B, Makowski MR. Diagnosis of Calcific Tendonitis of the Rotator Cuff by Using Susceptibility-weighted MR Imaging. Radiology. 2016 Feb;278(2):475-84. doi: 10.1148/radiol.2015150034. Epub 2015 Sep 3. PMID: 26347995.
16. Nörenberg D, Armbruster M, Bender YN, Walter T, Ebersberger HU, Diederichs G, Hamm B, Ockert B, Makowski MR. Diagnostic

performance of susceptibility-weighted magnetic resonance imaging for the assessment of sub-coracoacromial spurs causing subacromial impingement syndrome. Eur Radiol. 2017 Mar;27(3):1286-1294. doi: 10.1007/s00330-016-4441-0. Epub 2016 Jun 10. PMID: 27287483.

17. Bender YY, Diederichs G, Walter TC, Wagner M, Liebig T, Rickert M, Hermann KG, Hamm B, Makowski MR. Differentiation of Osteophytes and Disc Herniations in Spinal Radiculopathy Using Susceptibility-Weighted Magnetic Resonance Imaging. Invest Radiol. 2017 Feb;52(2):75-80. doi: 10.1097/RLI.0000000000000314. PMID: 27548342.

18. Bender YY, Böker SM, Diederichs G, Walter T, Wagner M, Fallenberg E, Liebig T, Rickert M, Hamm B, Makowski MR. MRI for the detection of calcific features of vertebral haemangioma. Clin Radiol. 2017 Aug;72(8):692.e1-692.e7. doi: 10.1016/j.crad.2017.02.018. Epub 2017 Mar 19. PMID: 28330684.

19. Ulas ST, Ziegeler K, Richter ST, Ohrndorf S, Poddubnyy D, Makowski MR, Diekhoff T. CT-like images in MRI improve specificity of erosion detection in patients with hand arthritis: a diagnostic accuracy study with CT as standard of reference. RMD Open. 2022 Feb;8(1):e002089. doi: 10.1136/rmdopen-2021-002089. PMID: 35177555; PMCID: PMC8860086.

20. Akhavi Milani A, Daghighi MH, Mirza-Aghazadeh-Attari M, Jalili J, Mahmoudpour M, Daghighi S. The diagnostic value of susceptibility-weighted imaging for identifying acute intraarticular hemorrhages. Skeletal Radiol. 2022 Sep;51(9):1777-1785. doi: 10.1007/s00256-022-04016-6. Epub 2022 Feb 25. PMID: 35212784.

21. Sieron DA, Drakopoulos D, Mitrakovic M, Tombarkiewicz M, Knap D, Platzek I, Tomalski M, Christe A. Assessment of 3-T MRI using susceptibility-weighted imaging to detect and evaluate intra- or periarticular blood metabolites and meniscal tears of the knee. Pol J Radiol. 2019 Sep 6;84:e340-e346. doi: 10.5114/pjr.2019.88480. PMID: 31969947; PMCID: PMC6964353.

22. Böker SM, Adams LC, Bender YY, Wagner M, Diekhoff T, Fallenberg E, Hamm B, Makowski MR. Evaluation of vertebral body fractures using susceptibility-weighted magnetic resonance imaging. Eur Radiol. 2018 May;28(5):2228-2235. doi: 10.1007/s00330-017-5195-z. Epub 2017 Dec 19. PMID: 29260364.

23. Liu J, Chen Y, Bao XM, Ling XL, Ding JP, Zhang ZK. [Study of susceptibility weighted imaging on MR and pathologic findings to distinguish benign or malignant soft tissue tumor]. Zhonghua Zhong Liu Za Zhi. 2017 May 23;39(5):350-354. Chinese. doi: 10.3760/cma.j.issn.0253-3766.2017.05.006. PMID: 28535651.

24. Nishibori H, Kato H, Kawaguchi M, Nagano A, Matsuo M. T2*-weighted MR imaging findings of giant cell tumors of bone: radiological-pathological correlation. Jpn J Radiol. 2019 Jun;37(6):473-480. doi: 10.1007/s11604-019-00829-z. Epub 2019 Mar 11. PMID: 30859458.

25. Dhillon M, Davies AM, Benham J, Evans N, Mangham DC, Grimer RJ. Calcific myonecrosis: a report of ten new cases with an emphasis on MR imaging. Eur Radiol. 2004 Nov;14(11):1974-9. doi: 10.1007/s00330-004-2368-3. Epub 2004 Oct 6. PMID: 15480695.

26. Valenzuela RF, Madewell JE, Kundra V, Costelloe CM. Advanced Imaging in Musculoskeletal Oncology: Moving Away From RECIST and Embracing Advanced Bone and Soft Tissue Tumor Imaging (ABASTI)-Part II-Novel Functional Imaging Techniques. Semin Ultrasound CT MR. 2021 Apr;42(2):215-227. doi: 10.1053/j.sult.2020.08.013. Epub 2020 Aug 29. PMID: 33814107.

27. Bush CH. The magnetic resonance imaging of musculoskeletal hemorrhage. Skeletal Radiol. 2000 Jan;29(1):1-9. doi: 10.1007/s002560050001. PMID: 10663582.

28. Sparacia G, Speciale C, Banco A, Bencivinni F, Midiri M. Accuracy of SWI sequences compared to T2*-weighted gradient echo sequences in the detection of cerebral cavernous malformations in the familial form. Neuroradiol J. 2016 Oct;29(5):326-35. doi: 10.1177/1971400916665376. Epub 2016 Aug 22. PMID: 27549150; PMCID: PMC5033099.

29. Hori M, Ishigame K, Kabasawa H. Pre- and postgadolinium enhanced susceptibility-weighted imaging at 1.5T for intracranial neoplasms: Contrast of pathologic lesions. Proc Intl Soc Mag Reson Med. 2007; 15:3764.

30. Valenzuela RF, Amini B, Duran-Sierra E, Canjirathinkal MA, Madewell JE. Multiparametric MRI for the Assessment of Treatment Effect and Tumor Recurrence in Soft tissue sarcoma of the Extremities. J Radiol Oncol. 2023; 7: 058-065. DOI: 10.29328/journal.jro.1001055

31. Adams LC, Bressem K, Böker SM, Bender YY, Nörenberg D, Hamm B, Makowski MR. Diagnostic performance of susceptibility-weighted magnetic resonance imaging for the detection of calcifications: A systematic review and meta-analysis. Sci Rep. 2017 Nov 14;7(1):15506. doi: 10.1038/s41598-017-15860-1. PMID: 29138506; PMCID: PMC5686169.

32. Zulfiqar M, Dumrongpisutikul N, Intrapiromkul J, Yousem DM. Detection of intratumoral calcification in oligodendrogliomas by susceptibility-weighted MR imaging. AJNR Am J Neuroradiol. 2012 May;33(5):858-64. doi: 10.3174/ajnr.A2862. Epub 2012 Jan 19. PMID: 22268093; PMCID: PMC7968798.

33. Child JR, Young CR, Amini B. Liposarcoma of the thigh with mixed calcification and ossification. Radiol Case Rep. 2016 Jul 1;11(3):217-21. doi: 10.1016/j.radcr.2016.05.010. PMID: 27594953; PMCID: PMC4996926.

34. Berberat J, Grobholz R, Boxheimer L, Rogers S, Remonda L, Roelcke U. Differentiation between calcification and hemorrhage in brain tumors using susceptibility-weighted imaging: a pilot study. AJR Am J Roentgenol. 2014 Apr;202(4):847-50. doi: 10.2214/AJR.13.10745. PMID: 24660715.

35. Wenaden AE, Szyszko TA, Saifuddin A. Imaging of periosteal reactions associated with focal lesions of bone. Clin Radiol. 2005 Apr;60(4):439-56. doi: 10.1016/j.crad.2004.08.017. PMID: 15767101.

36. Ghosh PS, Ghosh D. Teaching neuroimages: MRI "target sign" and neurofibromatosis type 1. Neurology. 2012 Feb 28;78(9):e63. doi: 10.1212/WNL.0b013e318248df63. PMID: 22371419.

37. Fox MG, Bancroft LW, Peterson JJ, Kransdorf MJ, Terkonda SP, O'Connor MI. MRI appearance of myocutaneous flaps commonly used in orthopedic reconstructive surgery. AJR Am J Roentgenol. 2006 Sep;187(3):800-6. doi: 10.2214/AJR.05.0484. PMID: 16928948.

38. Knowles NG, Smith DL, Outwater EK. MRI diagnosis of brown tumor based on magnetic susceptibility. J Magn Reson Imaging. 2008 Sep;28(3):759-61. doi: 10.1002/jmri.21441. PMID: 18777537.

39. Carvalho R, Kurochka S, Rocha J, Fernandes JS. Brown tumor of the mandible: Magnetic susceptibility demonstrated by MRI. Radiol Case Rep. 2015 Dec 7;7(2):662. doi: 10.2484/rcr.v7i2.662. PMID: 27326285; PMCID: PMC4899808.

40. Valenzuela RF, Sierra ED, Canjirathinkal MA, Costelloe CM, Madewell JE, Murphy WA, Amini B. Early results in the novel use of contrast-enhanced susceptibility-weighted imaging in the assessment of response and progression in desmoid fibromatosis: A pilot study in a specialized cancer institution. Tumor Discovery. 2023; 2(3): 1414. https://doi.org/10.36922/td.1414

41. Wardelmann E, Haas RL, Bovée JV, Terrier P, Lazar A, Messiou C, LePechoux C, Hartmann W, Collin F, Fisher C, Mechtersheimer G, DeiTos AP, Stacchiotti S, Jones RL, Gronchi A, Bonvalot S. Evaluation of response after neoadjuvant treatment in soft tissue sarcomas; the European Organization for Research and Treatment of Cancer-Soft Tissue and Bone Sarcoma Group (EORTC-STBSG) recommendations for pathological examination and reporting. Eur J Cancer. 2016 Jan;53:84-95. doi: 10.1016/j.ejca.2015.09.021. Epub 2015 Dec 14. PMID: 26700077.

42. Eckhardt BP, Hernandez RJ. Pigmented villonodular synovitis: MR imaging in pediatric patients. Pediatr Radiol. 2004 Dec;34(12):943-7. doi: 10.1007/s00247-004-1261-1. Epub 2004 Sep 22. PMID: 15448943.